Article

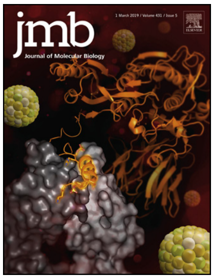

Aggregation of Respiratory Complex Subunits Marks the Onset of Proteotoxicity in Proteasome Inhibited Cells

Shivali Rawat, Valpadashi Anusha, Manoranjan Jha,
K. Sreedurgalakshmi and Swasti Raychaudhuri

CSIR-Centre for Cellular and Molecular Biology, *Uppal Road, Hyderabad 500007, India*

Correspondence to Swasti Raychaudhuri: *rcswasti@ccmb.res.in*

https://doi.org/10.1016/j.jmb.2019.01.022
Edited by J. Buchner

Abstract

Proteostasis is maintained by optimal expression, folding, transport, and clearance of proteins. Deregulation of any of these processes triggers protein aggregation and is implicated in many age-related pathologies. In this study, using quantitative proteomics and microscopy, we show that aggregation of many nuclear-encoded mitochondrial proteins is an early protein destabilization event during short-term proteasome inhibition. Among these, respiratory chain complex (RCC) subunits represent a group of functionally related proteins consistently forming aggregates under multiple proteostasis stresses with varying aggregation propensities. Sequence analysis reveals that several RCC subunits, irrespective of the cleavable mitochondrial targeting sequence, contain low-complexity regions at the N-terminus. Using different chimeric and mutant constructs, we show that these low-complexity regions partially contribute to the intrinsic instability of multiple RCC subunits. Taken together, we propose that physicochemically driven aggregation of unassembled RCC subunits destabilizes their functional assembly inside mitochondria. This eventually deregulates the biogenesis of respiratory complexes and marks the onset of mitochondrial dysfunction.

Introduction

Any physicochemical stress that perturbs protein conformation is capable of triggering its misfolding and aggregation. Heat stress unfolds protein secondary structure, exposes its hydrophobic stretches, and results in the formation of either reversible or amyloidogenic aggregates [1,2]. Perturbation of protein homeostasis (proteostasis) network also promotes aggregation as the balance between abundance and intrinsic solubility of proteins is lost [3]. The identity of destabilized proteins and magnitude of instability may vary depending on the mechanism of proteostasis stress. Moreover, perturbing the same node of proteostasis network may trigger differential conformational collapse and aggregation in distinct groups of proteins in a condition-specific manner. For example, members of Hsp70 chaperone family normally prevent unproductive folding of hydrophobic stretches in newly synthesized proteins. On the other hand, reduced availability of the same chaperones in stressed cells decelerates the refolding of mature yet unfolded proteins and enhances aggregation [4]. Predominantly, aggregated proteins cannot perform normal function owing to their loss of conformation and are often implicated in various pathologies. However, protein aggregation may not always be deleterious. Multiple studies have suggested transient aggregation of proteins as a part of cellular defense [1,2,5].

Earlier studies had investigated global proteome changes in proteostasis stressed cells along with protein aggregation events to certain but limited extent. Large-scale proteomic studies in proteasome inhibited cells had previously identified several short-lived proteins, delineated compartment-specific protein degradation mechanisms, and established the role of multiple chaperones and ubiquitin ligases in clearing insoluble proteins [6–9]. On the other hand, ER stress was shown to cause widespread amorphous and amyloidogenic aggregation in cytosol [10], while Hsp90 inhibition preferentially affected kinases and proteins involved in DNA damage response [11]. Despite these studies, whether protein aggregation at early phases of proteostasis stress is widespread and stochastic in occurrence or is determined by physicochemical or functional properties that forces specific group of proteins to aggregate due to a slight perturbation of proteostasis remains to be investigated. Moreover, how these initial protein aggregation events contribute to cellular protection or collapse during prolonged stress is not yet extensively studied. Since malfunction of proteasome significantly contributes to proteotoxicity in neurons [12], we selected the fast-growing mouse neuroblastoma cell-line Neuro2a for our study and used proteasome inhibitor and other small molecules to identify the most vulnerable proteins that form aggregates at early stages of proteostasis stresses.

Using quantitative proteomics, we find that nuclear-encoded mitochondrial proteins over-represent the list of proteins that partition from soluble to insoluble fraction at an early stage of proteasome inhibition. Among these, respiratory chain complex (RCC) subunits, which constitute multi-protein functional complexes inside mitochondria, represent a set of proteins forming aggregates due to multiple proteostasis stresses. Intrinsic instability of RCC subunits is determined by diverse physicochemical properties including low-complexity regions (LCRs) at N-termini; sequence stretches containing repeats of single amino acids or short amino acid motifs. These N-terminal regions also code for targeting sequences in multiple RCC subunits that drive their translocation and functional association into respiratory complexes inside mitochondria. Together, we propose that aggregation of RCC subunits highlights an early proteotoxic signature that impedes respiratory chain function during prolonged stress.

Results

Destabilization of chaperone-dependent proteins at early phase of proteasome inhibition

To establish a stress condition that triggers aggregation of proteostasis-sensitive proteins without altering viability, we treated Neuro2a cells with cell-permeable proteasome inhibitor MG132 [13]. Earlier, an 8-h treatment in HeLa cells with 5 μM MG132 was shown to trigger formation of small inclusion bodies (IBs) of proteostasis-sensitive protein FlucDM-EGFP, firefly luciferase with double mutations (FlucDM), a conformationally unstable, chaperone-dependent protein [14]. In this study, 5 μM and even 2.5 μM MG132 were found to efficiently block proteasome activity in Neuro2a cells with increased load of ubiquitinated proteins after 8 h without any loss of cell viability (Figs. 1a and S1a–c). In untreated cells, transfected FlucDM-EGFP was diffusely distributed all throughout with a few small dispersed IBs. Treatment with both 2.5 and 5 μM MG132 resulted in larger IBs after 8 h (Fig. 1b). To confirm whether FlucDM-EGFP IBs partitioned from soluble to insoluble fraction, we lysed the cells using a mild lysis buffer that solubilizes most of the cellular proteins including components of various organelles while retaining the aggregated proteins as pellet (Fig. S1d and e). Total fraction was prepared by dissolving the cells directly in SDS lysis buffer. Western blot analysis confirmed increased load of FlucDM-EGFP in the total fraction due to reduced degradation in the presence of MG132 and subsequent precipitation into insoluble fraction. No change in protein level was observed in the soluble fraction (Fig. S1f). However, simultaneous drop in luminescence activity suggested dose-dependent instability of the soluble FlucDM-EGFP (Fig. 1c).

Accumulation of protein aggregates in the cytoplasm is known to trigger defense mechanisms like heat shock factor 1 (Hsf1)-mediated cytosolic stress response (or heat shock response). Hsf1 was activated by 8-h MG132 treatment of Neuro2a cells as observed by an upshifted phosphorylated protein band suggesting the appearance of cytosolic aggregates of endogenous proteins (Fig. 1d) [15]. Simultaneous increase in mRNA levels of hsp70 (hspa1b) and Ubiquitin (ubc) genes corroborated the upregulation of Hsf1-mediated transcription (Fig. 1e). The upshifted Hsf1 band started migrating to its original position by 24 h illustrating the reversal of the trans-activation mechanism during prolonged stress (Fig. 1d).

Autophagy has been reported to be induced in proteasome-inhibited cells as a backup mechanism for clearance of misfolded protein [16,17]. In our experiments, an increased cleavage of LC3 indicating activation of autophagy was observed only by 24 h of MG132 treatment, whereas uncleaved version was prominent after 8 h (Fig. 1d). It is noteworthy that a significant reduction in cell viability was also observed after 24 h, implying that adaptive rescue mechanisms were not sufficient to protect cells during long-term proteasome inhibition (Figs. 1a and S1a). Thus, 8 h of MG132 treatment represented an early time point when highly unstable proteins start partitioning into insoluble fraction and initiate proteotoxicity, while the cellular functions remain mostly unaffected and adaptive mechanisms are initiated after sensing the minute equilibrium shift in proteome. Our next goal was to identify the endogenous proteins that are unstable and aggregation-prone at this early stage of proteostasis stress.

Proteome reorganization at early stages of proteasome inhibition

Proteostasis-sensitive protein FlucDM-EGFP showed dose-dependent loss of activity with MG132 treatment (Fig. 1c). Increase in hspa1b mRNA level due to MG132 treatment was also significantly dose dependent (Fig. 1e). Both these results indicated possible differences in proteome destabilization events with increasing concentrations of MG132. Hence, we investigated proteome partitioning from

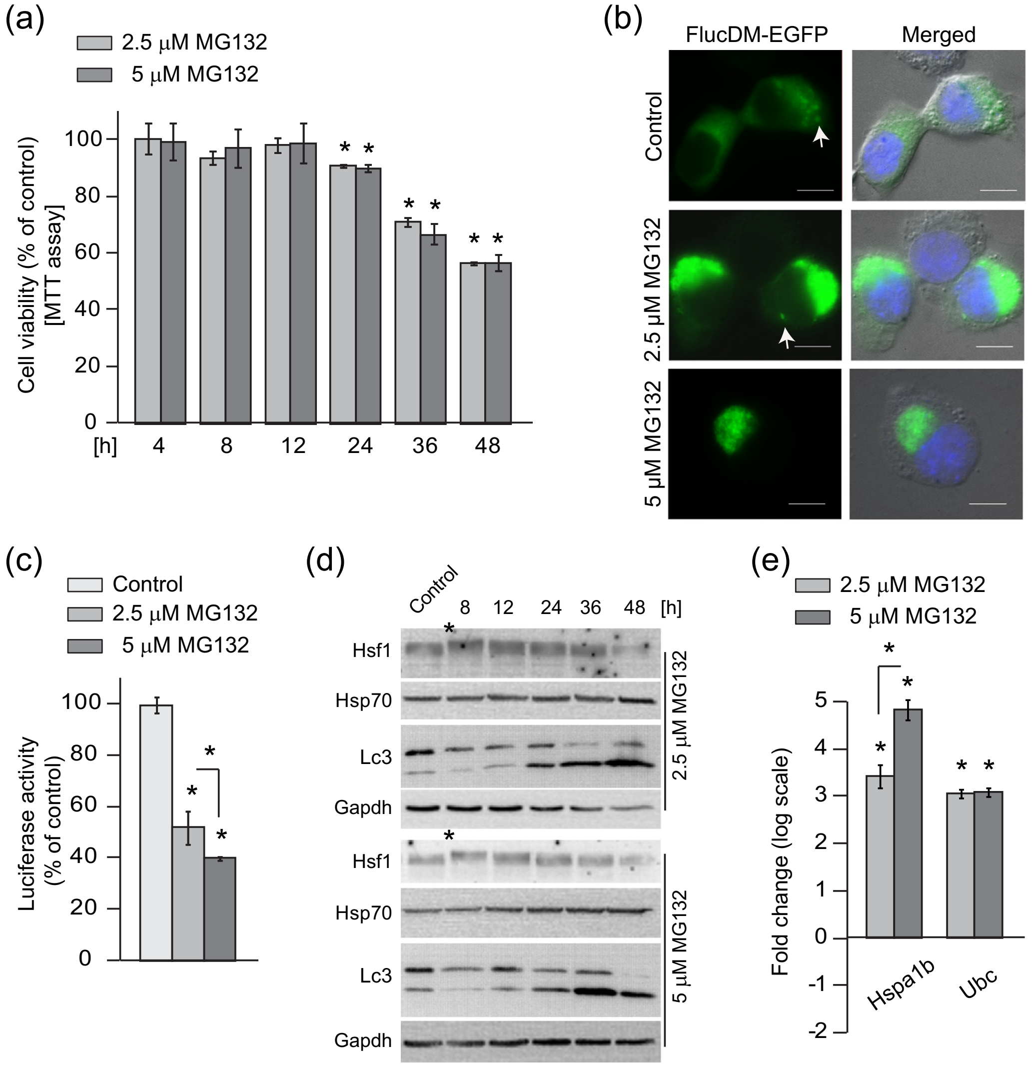

Fig. 1. Destabilization of chaperone-dependent proteins in Neuro2a cells by short-term proteasome inhibition. (a) Cell viability. Neuro2a cells were incubated with MG132 and cell viability was estimated by MTT assay. Control: DMSO-treated cells. Error bars indicate SDs from at least three independent experiments. * indicates $p < 0.05$ by Student's *t* test. (b) Fluorescence micrographs showing IBs formed by over-expressed FlucDM-EGFP in MG132-treated Neuro2a cells for 8 h. Nucleus is stained by DAPI. Arrows indicate smaller IBs. Control: DMSO-treated cells. The scale bar represents 10 μm. (c) FlucDM activity assay. Luciferase activity was measured in FlucDM-EGFP-transfected cells as described in Materials and Methods. Control: DMSO-treated cells. Error bars indicate SDs from at least three independent experiments. * indicates $p < 0.05$ by Student's *t* test. (d) Hsp70, Hsf1, and Lc3 protein levels in MG132-treated cells. Neuro2a cells were treated with MG132 for different time lengths, soluble extracts were prepared, and immunoblot was performed with anti-Hsp70, anti-Hsf1, anti-Lc3, and anti-GAPDH. * indicates upshifted band of Hsf1. Extract of DMSO-treated cells was used as control. Gapdh served as loading control. (e) Hsp70 and ubiquitin mRNA levels in MG132-treated cells for 8 h as determined by real-time PCR. Fold change was normalized against mRNA levels in DMSO-treated cells. Error bars indicate SDs from at least three independent experiments. * indicates $p < 0.05$ by Student's *t* test.

soluble to insoluble fraction in both 2.5 and 5 μM MG132 treated Neuro2a cells. Overall, we identified 1986, 1329, and 838 proteins, respectively, in the total, soluble, and insoluble fractions using SILAC-based quantitative mass spectrometry (Figs. 2a and S2a; Table S1). The proteins identified in the insoluble fraction were physicochemically distinct with basic isoelectric point (p*I*), increased frequency of LCRs, were more number of positively charged residues, and were more abundant as per iBAQ analysis when compared to all proteins identified in the total and soluble fractions (Fig. S2b). Contrary to the general perception that membrane association causes proteins to precipitate [18,19], a relatively small number of transmembrane helix containing proteins were present in the insoluble fraction (Fig. S2c).

The SILAC ratios, reflecting the relative abundance of proteins before and after MG132 treatment, were log

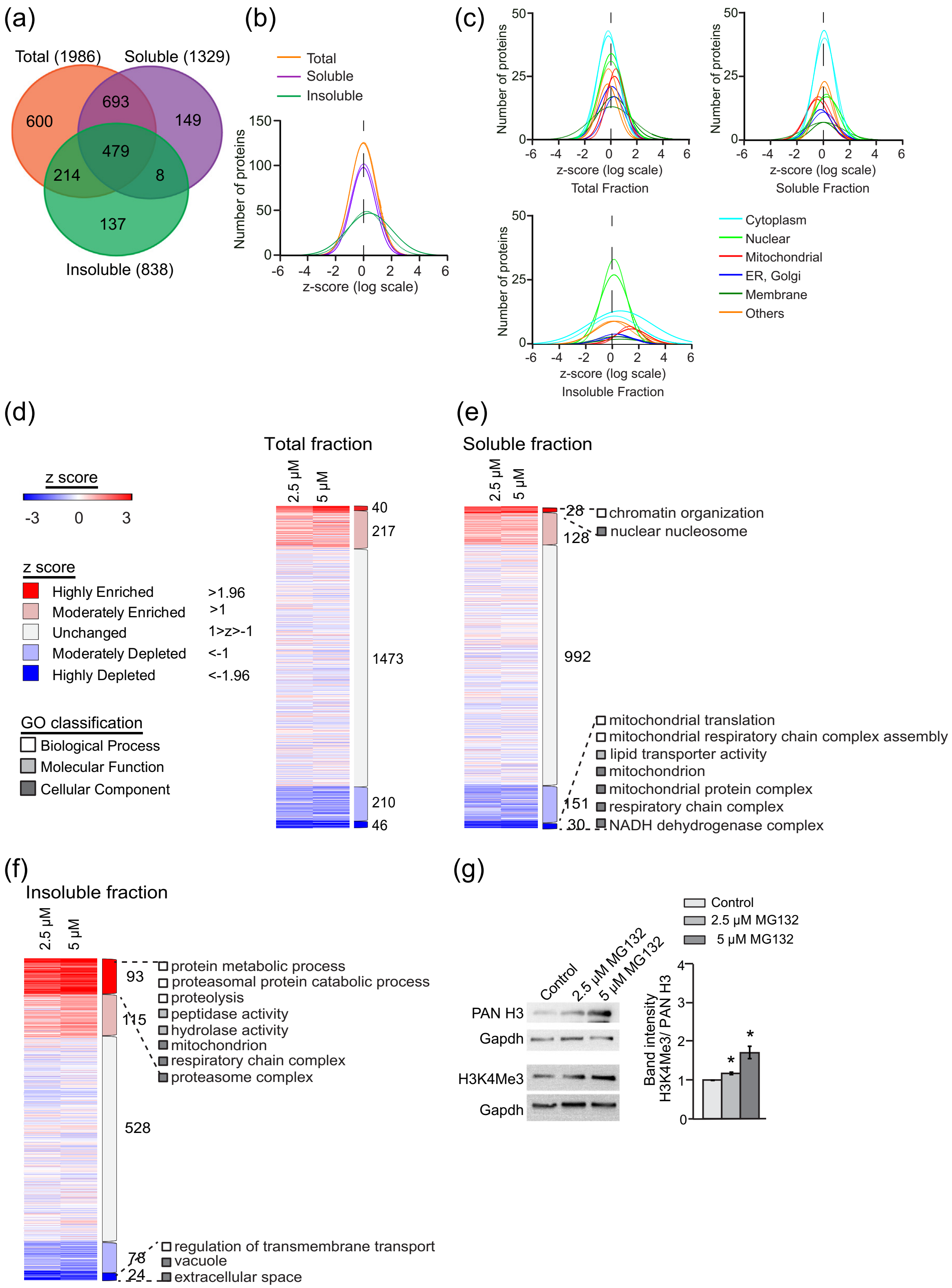

Fig. 2 (*legend on next page*)

transformed and converted into *z*-scores. We observed normal distribution profile of *z*-scores for both total and soluble fractions, with only few outliers indicating the enriched or depleted proteins due to MG132 treatment. Since the insoluble fraction showed a skewed distribution of *z*-scores (Fig. 2b), it was normalized with respect to the mean and standard deviation of total fraction (see Materials and Methods for detail). Next, we divided the quantified proteins in multiple groups according to their redistribution profile in the MG132-treated cells. Comparison of *z*-score distribution profiles of proteins from different sub-cellular localization (as predicted by UniProt) suggested enrichment of mitochondrial proteins in the total fraction. In the soluble fraction, distribution profile of mitochondrial proteins indicated a shift toward depletion. Slight shift in *z*-scores was observed for all quantified proteins in the insoluble fraction, thereby indicating an increase in protein aggregation due to proteasome inhibition. Among these, increase in *z*-scores for mitochondrial proteins was the highest (Fig. 2c).

Next, a cutoff of 95% confidence, which corresponds to *z*-scores beyond ± 1.96 in either 2.5- or 5-μM treatment, was used to identify the highly enriched or depleted proteins [20]. Only 14 and 10 proteins, respectively, were found to be highly enriched consistently with both the concentrations of MG132 in the total and soluble fractions. Similarly, only 17 and 16 proteins were highly depleted in these fractions, respectively (Tables S1a and S1b). Multiple proteins were significantly altered in either of the MG132 concentrations and showed similar but non-significant trend at the other dose. This finding indicates the subtle fluctuations in proteome equilibrium at early stages of proteasome inhibition that are dynamic, yet following a consistent trend. Including these proteins, the number of highly enriched proteins increased to 40 and 28 and highly depleted proteins to 46 and 30 in total and soluble fractions, respectively (Fig. 2d and e; Tables S1a and S1b). Furthermore, we identified 60 proteins with *z*-score beyond + 1.96 with both treatments, and 93 with either of the treatments in insoluble fraction, indicating a general tendency of most proteins toward insolubility. In contrast, 24 proteins showed *z*-scores below − 1.96 with 8 common between the treatments (Fig. 2f, Table S1c).

Ubiquitin load was highly increased in all the fractions with MG132 treatment (Table S1). The enriched or depleted proteins in the total fraction did not represent any significant Gene Ontology (GO) class (Fig. 2d and Table S1a). GO analysis of the highly enriched proteins in the soluble fraction contained many "chromatin organization" (GO:0006325) proteins including histones H3 and H4 (Fig. 2e; Tables S1b and S1b). This could be suggestive of transcriptional reorganization since we also observed increased level of active transcription mark H3K4me3 in MG132-treated cells (Fig. 2g). Indeed, increased H3K4Me3 at the hsp70 promoter region has been reported to be an adaptive active transcription mark against proteotoxicity triggered by heat stress [21]. On the other hand, highly depleted proteins in soluble fraction were represented by GO terms "mitochondrion" (GO:0005739), "respiratory chain complex" (GO:0098803), and "mitochondrial translation" (GO:0032543; Table S2b). Simultaneously, many proteins representing the GO class "respiratory chain complex" (GO:0098803) were among the highly enriched proteins in the insoluble fraction, thus suggesting their increased aggregation propensity with MG132 treatment (Fig. 2e and f; Tables S1b and S1c). In contrast, highly depleted proteins in the insoluble fraction represented "extracellular space" (GO:0005615) and "vacuole" (GO:0005773) related proteins. Several proteins that were found to be depleted in the total fraction are also cataloged as "exosome components" or "secreted" in the Exocarta database [22] (Fig. 2f and Table S1) suggesting protein secretion as a possible mechanism of quality control at early stages of proteasome inhibition [23].

The other proteins enriched in the insoluble fraction included many ubiquitin proteasome system (UPS) components (Fig. 2f), similar to that described earlier [6]. Strikingly, except for a few specialized chaperones, we did not observe substantial increase in common stress-responsive chaperone levels in any fraction after the 8-h MG132 treatment (Fig. S2d). In the total fraction, Dnajb6, a chaperone involved in suppressing aggregation and toxicity of neuronal amyloid proteins [24] and Bcs1l, an assembly factor of mitochondrial RCC III [25] showed tendency toward enrichment. In the soluble fraction, Bag6 was significantly increased with both treatments. Bag6 is an ATP-independent chaperone that prevents aggregation of misfolded and hydrophobic patch containing proteins and is also required for the selective ubiquitin-mediated

Fig. 2. Proteome reorganization in response to short-term proteasome inhibition. (a) Venn diagram showing overlap between the quantified proteins in total, soluble, and insoluble fractions of MG132-treated Neuro2a cells for 8 h. (b) Histogram of *z*-score distribution of quantified proteins across proteome fractions. (c) Histogram of *z*-score distribution of proteins based on their sub-cellular localization (as curated from Uniprot). Solid line for 5 μM MG132 and dashed line for 2.5-μM MG132 treatment. (d) *z*-Score distribution of the quantified proteins in the total fraction. No GO class significantly represented the enriched or depleted proteins. (e and f) *z*-Score distribution of the quantified proteins in the soluble fraction and insoluble fraction. Significant GO classes representing the highly enriched and highly depleted proteins are shown. Color scheme similar as panel d. (g) Western blots showing Histone H3 and H3K4Me3 levels in the total fraction. Band intensities were normalized to pan Histone H3 protein levels. Extract of DMSO-treated cells served as control. Error bars indicate SDs from at least three independent experiments. * indicates $p < 0.05$ by Student's *t* test.

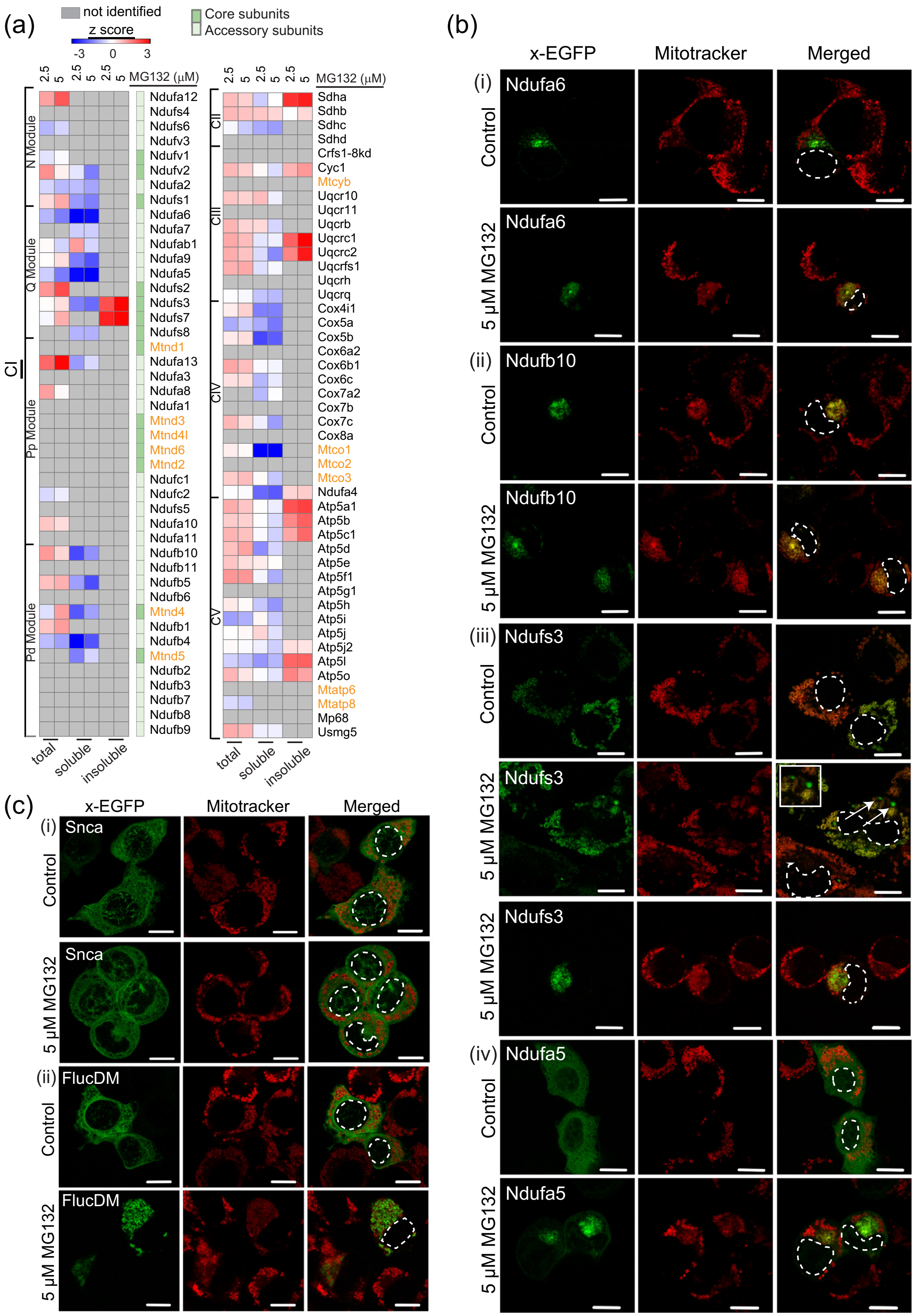

Fig. 3 (*legend on next page*)

degradation of defective nascent chain polypeptides by the proteasome [26]. In addition, Dnajc19, a putative component of TIM23 complex-associated import motor that drives the transport of precursor proteins into mitochondria [27], was significantly enriched only by 2.5-μM treatment. Dnajb2, a co-chaperone of the HSP70 family [28], was identified as highly enriched in the insoluble fraction after 5-μM treatment (Fig. S2d and Table S1). ER chaperone Grp78 and mitochondrial Hsp60 were identified in all the fractions but without any change with proteasome inhibition. Inducible forms of cytosolic chaperone Hsp70, namely, Hspa1a and Hspa1b, were not identified by mass spectrometry, while the constitutive form Hsc70 remained unchanged consistent with our immunoblot that shows no increase in HSP70 levels by 8-h MG132 treatment (Fig. 1d). Other common cytosolic chaperones such as Hsp90aa1, Hsp90ab1, and Hsp90b1 and components of TRiC chaperonin machinery were also identified across the fractions although remained unchanged with proteasome inhibition (Fig. S2d and Table S1).

Taken together, consistent precipitation of multiple mitochondrial proteins from soluble to insoluble fraction highlighted the early protein destabilization events during proteasome inhibition. Aggregation of mitochondrial proteins is not uncommon. Recently, many mitochondrial precursor proteins have been shown to be sequestered within the cytosolic aggregates of huntingtin [29]. Nuclear-encoded mitochondrial proteins have also been found in age-related aggregates [30]. In our experiments, RCC subunits represented the most prominent group of aggregation prone mitochondrial proteins. Therefore, we focused on further investigating the aggregation propensity of the RCC subunits, the physicochemical features driving their aggregation, and the functional consequences.

Redistribution of RCC subunits

Total fraction

Among the 56 RCC subunits identified in the total fraction, three RCC I (CI) were highly enriched by 5-μM treatment and moderately enriched by 2.5-μM treatment (Fig. 3a and Table S3a). When we reduced the statistical stringency of data analysis, 14 more RCC subunits (6 CI, 3 CIII, 1 CIV, and 4 CV) populated the list of "moderately enriched" proteins (Table S3a) indicating their lack of degradation during MG132 treatment. Interestingly, three CI subunits (Ndufa5, Ndufa6, and Ndufb4) and one CV subunit (Atp5i) were found to be moderately depleted in the total fraction implying either secretion or degradation via unknown proteases.

Soluble fraction

In the soluble fraction, 49 RCC subunits were identified (Table S3b). CI component Ndufab1 was the only moderately enriched RCC subunit. On the other hand, six CI and two CIV subunits were highly depleted in the soluble proteome with either of the treatments, and these included three mitoribosome components (Fig. 3a and Table S3b). Sixteen more RCC subunits and three mitoribosome components were among the moderately depleted proteins (Table S3b). In the absence of transcriptional downregulation as confirmed by RT-PCR experiments (Fig. S2e), the RCC subunits were either partitioned into the insoluble fraction or secreted or degraded by some unconventional mechanism.

Insoluble fraction

In the insoluble fraction, 14 RCC subunits were identified, among which 6 were highly enriched and included 2 CI, 1 CII, 2 CIII, and 1 CV subunits. Five RCC subunits were present as moderately enriched including one CIII and four CV components (Fig. 3a and Table S3c).

Aggregation of RCC subunits

To investigate the aggregation propensity of RCC subunits in proteasome-inhibited cells, we tagged EGFP to four CI-subunits Ndufs3, Ndufa5, Ndufa6, and Ndufb10 that were highly depleted in soluble fraction. Ndufs3 was also highly enriched in insoluble fraction. In the insoluble fraction, aggregation propensity of multiple RCC subunits was more prominent upon 5-μM MG132 treatment (Fig. 3a and Table S3c), and we used the same concentration for the microscopy experiments. Over-expression of Ndufa6 and Ndufb10 resulted in spontaneous aggregation even in the absence of proteasome inhibition suggesting their high aggregation propensity (Fig. 3bi and bii). As reported earlier, over-expression of fluorescent reporter-tagged Ndufs3 neither forms aggregates nor perturbs CI assembly and function in HEK293 cells [31]. Similarly, over-expressed Ndufs3-EGFP did not form aggregates in Neuro2a cells and was largely targeted to mitochondria. However, consistent

Fig. 3. Aggregation of RCC subunits by short-term proteasome inhibition. (a) Heatmap showing *z*-score distribution of RCC subunits across the proteome fractions of MG132-treated Neuro2a cells for 8 h. Mitochondria-encoded subunits are shown in orange. (b) Fluorescence micrographs showing aggregate formation by overexpressed C-terminal EGFP-tagged RCC subunits (x-EGFP) with MG132 for 8 h. Arrows indicate smaller IBs shown in zoomed insets. (c) Fluorescence micrographs showing overexpressed C-terminal EGFP-tagged control proteins (x-EGFP) with MG132 for 8 h. Mitochondria are stained by Mitotracker CMXRos (red). Cell fixation was performed using acetone-methanol. Nucleus is shown by dotted lines. Control: DMSO-treated cell. The scale bar represents 10 μm.

with our mass spectrometry observations, multiple distinct mitotracker negative IBs appeared in many cells upon 8-h MG132 treatment (Fig. 3biii). Moreover, we observed disorganized mitochondrial staining along with larger Ndufs3 aggregates in several cells, indicating that the aggregating RCC subunits could either be inside mitochondria or in the cytosol or bound to the outer surface of mitochondria as described recently by Weidberg and Amon [32] (Fig. 3biii, bottom panels). The other RCC subunit

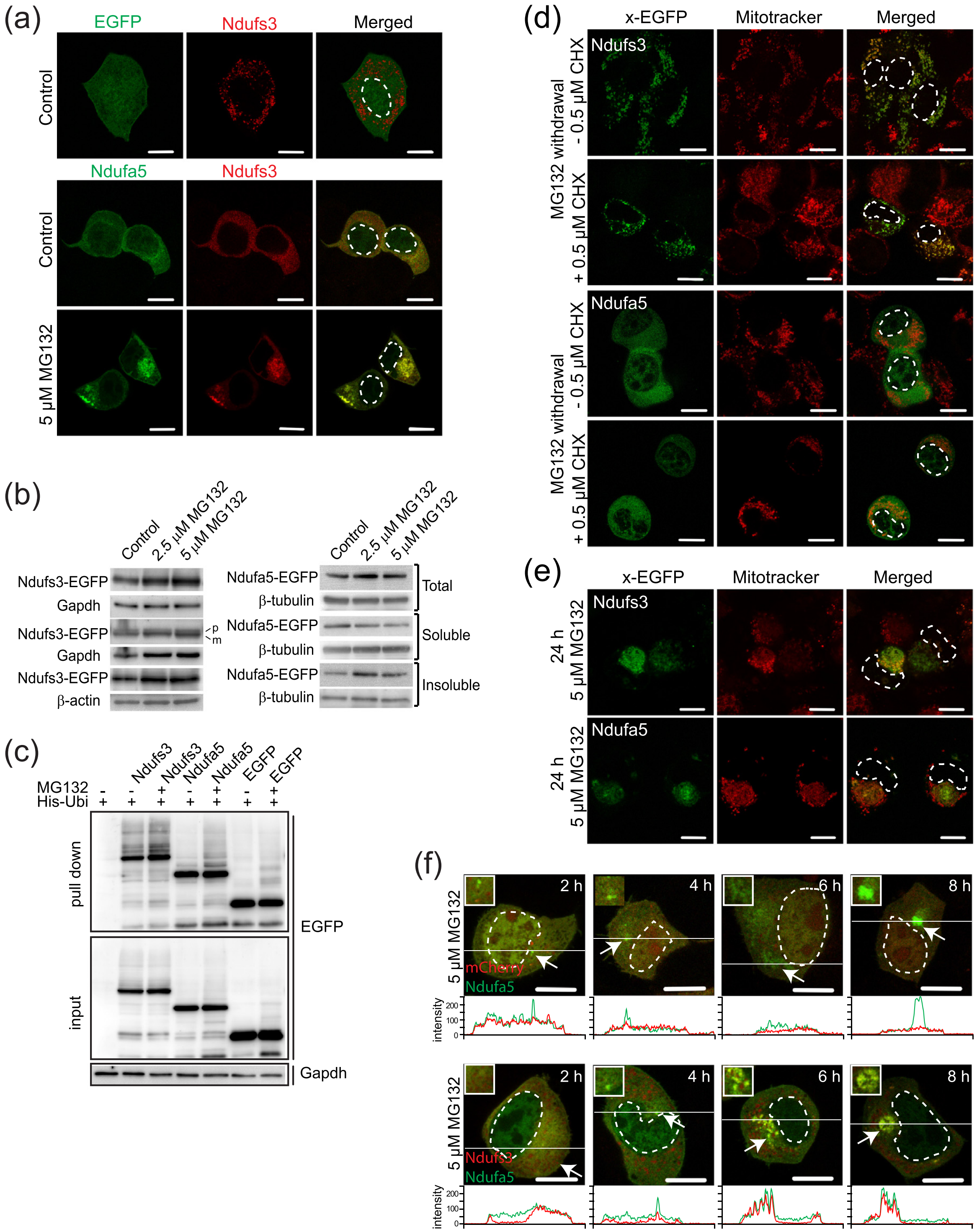

Fig. 4 (*legend on next page*)

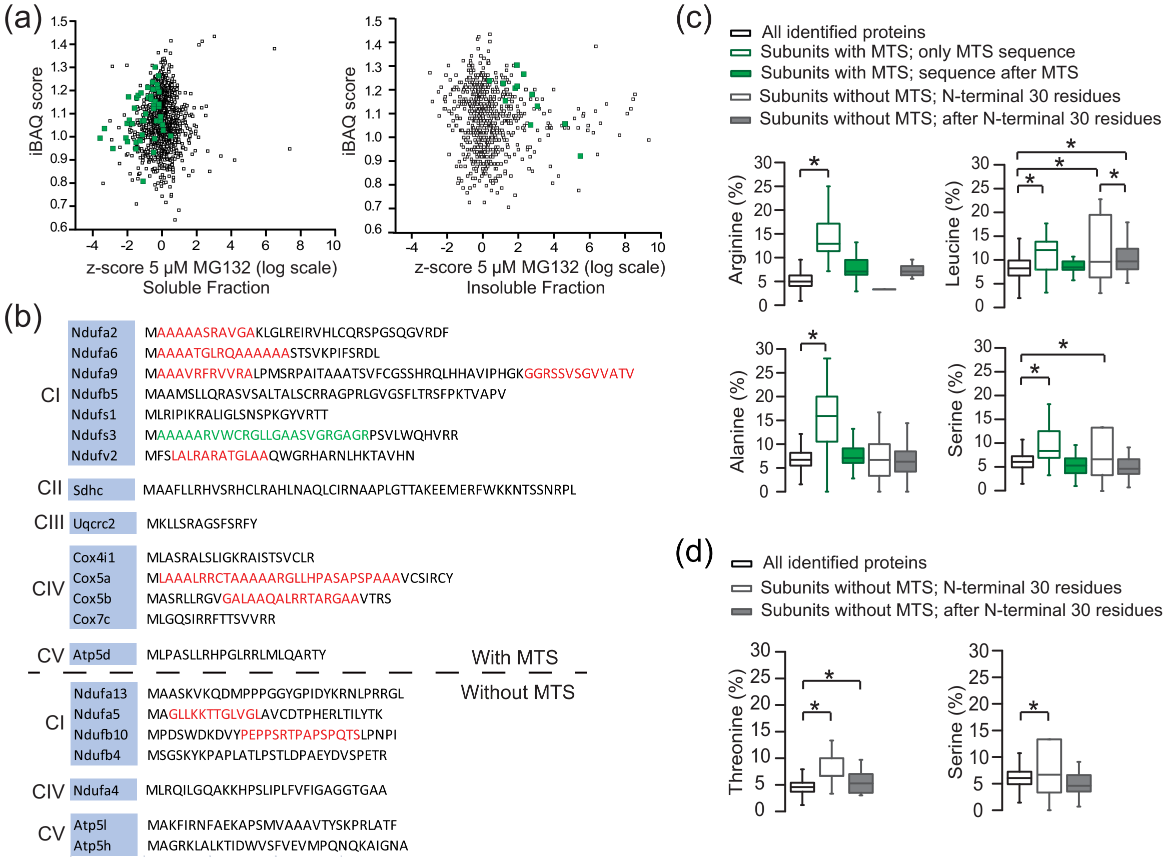

Fig. 5. Physicochemical properties of nuclear-encoded RCC subunits in aggregation. (a) Scatter plot of iBAQ scores as calculated from total fraction *versus* z-score distribution in soluble and insoluble fraction. Green solid squares indicate RCC subunits, and black hollow squares are other identified proteins. (b) LCRs in the predicted MTS or N-terminal 30 residues of nuclear-encoded RCC subunits depleted in the soluble fraction. High confidence LCRs are highlighted in red; low confidence, in green. (c) Box plots showing amino acid composition of MTS of RCC subunits. MTS or N-terminal 30 residues and the rest of the protein sequences are grouped separately. * indicates $p < 0.05$ by one-way ANOVA, Bonferroni's post hoc test. (d) Box plots showing amino acid composition of identified RCC subunits without MTS. N-terminal 30 residues and the rest of the protein sequences are grouped separately. * indicates $p < 0.05$ by one-way ANOVA, Bonferroni's post hoc test.

Ndufa5 does not contain a conventional mitochondrial targeting sequence (MTS) as predicted by TPpred2 [33]. Over-expressed Ndufa5-EGFP displayed diffused distribution throughout the cell and was sequestered into aggregates nearby nucleus with slight mitotracker co-staining after MG132 treatment (Fig. 3biv). In contrast, a non-mitochondrial protein α-synuclein (Snca-EGFP) neither formed

Fig. 4. Aggregation of RCC subunits by short-term proteasome inhibition. (a) Microscopy images of Ndufs3-mCherry co-transfected with EGFP or Ndufa5-EGFP. Cell fixation was performed using paraformaldehyde. Control: DMSO-treated cell. (b) Ubiquitylation of RCC subunits. Neuro2a cells were transfected with His-ubiquitin (His-Ubi) and Ndufs3-EGFP or Ndufa5-EGFP or EGFP. After 24 h, cells were treated with 5 μM MG132 or DMSO. Cells were lysed and His-Ubi pull-down performed. Samples were separated by SDS-PAGE and immunoblotted with anti-EGFP. (c) Redistribution of overexpressed Ndufs3-EGFP and Ndufa5-EGFP in total, soluble, and insoluble fraction. "p" and "m" indicate precursor and mature protein band, respectively. Gapdh served as loading control for total and soluble fraction; β-actin, for insoluble fraction for Ndufs3-EGFP; and β-tubulin, for Ndufa5-EGFP. (d) Microscopy images showing reversal of Ndufs3-EGFP and Ndufa5-EGFP aggregates. MG132 was withdrawn after 8 h of treatment and recovery was done for 16 h in fresh culture media with and without CHX. Mitochondria are stained by Mitotracker CMXRos (red). Cell fixation was performed using acetone-methanol. (e) Fluorescence micrographs showing continued aggregation by overexpressed C-terminal EGFP-tagged RCC subunits (x-EGFP) with MG132 after 24 h. Mitochondria are stained by Mitotracker CMXRos (red). Cell fixation was performed using acetone-methanol. (f) Microscopy images of Ndufa5-EGFP co-transfected with mCherry or Ndufs3-mCherry. Cells were treated with MG132 for indicated time points. Cell fixation was performed using paraformaldehyde. Fluorescence intensity profile along the line is shown. Arrows indicate ROI shown in zoomed insets. Nucleus is shown by dotted lines in all microscopy images. The scale bar represents 10 μm.

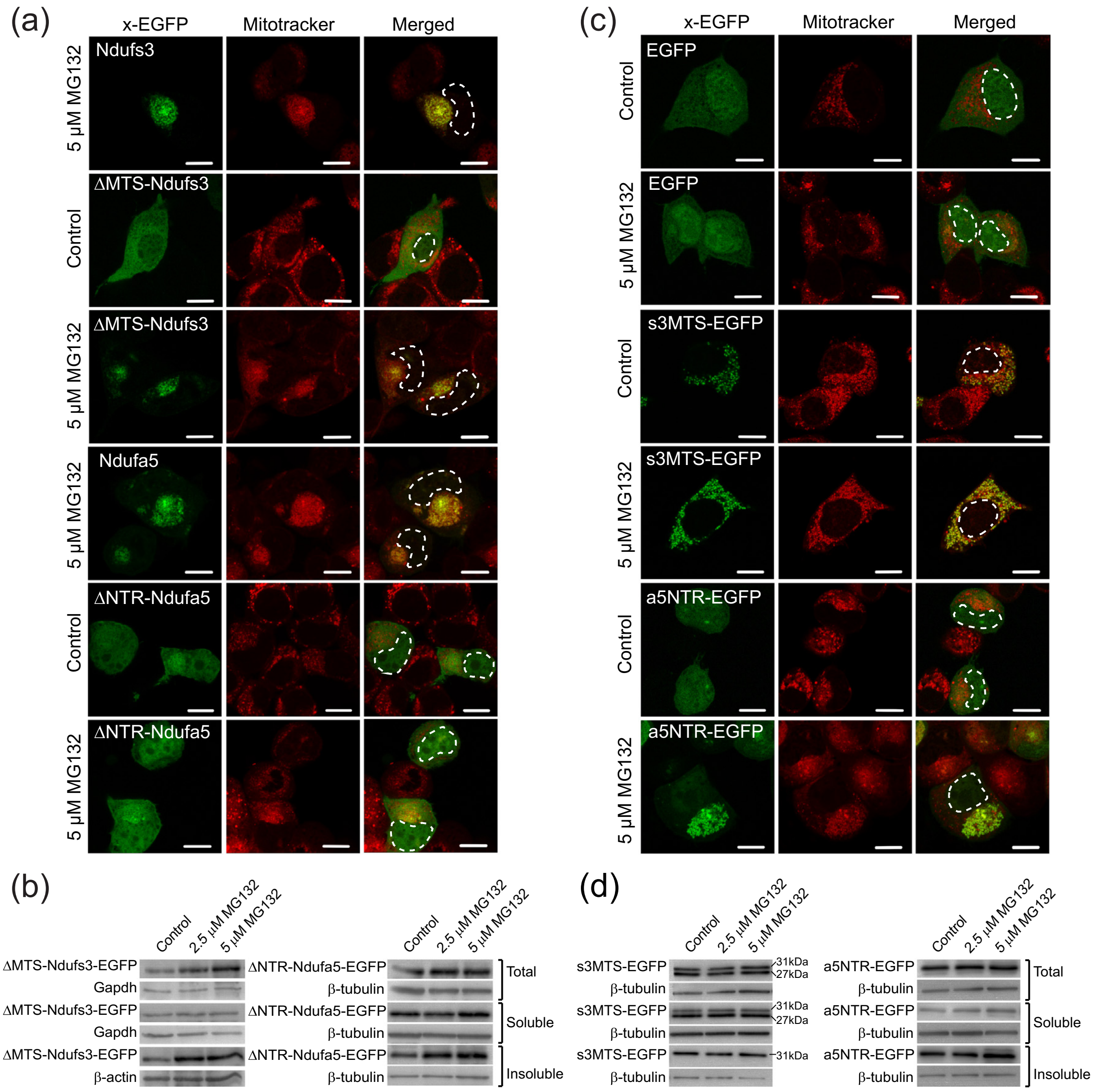

Fig. 6. Role of LCR containing N-terminal regions of RCC subunits in aggregation. (a) Fluorescence micrographs of ΔMTS-Ndufs3-EGFP and ΔNTR-Ndufa5-EGFP with 8-h treatment. Cell fixation was performed using paraformaldehyde. Nucleus is shown by dotted lines. Control: DMSO-treated cells. The scale bar represents 10 µm. (b) Redistribution of overexpressed ΔMTS-Ndufs3-EGFP and ΔNTR-Ndufa5-EGFP in total, soluble, and insoluble fraction. Gapdh served as loading control for total and soluble fraction; β-actin, for insoluble fraction for ΔNdufs3-EGFP; β-tubulin, for ΔNdufa5-EGFP. (c) Fluorescence micrographs of EGFP with MTS of Ndufs3 and NTR of Ndufa5 with 8 h treatment. Mitochondria are stained by Mitotracker CMXRos (red). Cell fixation was performed using paraformaldehyde. Nucleus is shown by dotted lines. Arrows indicate smaller IBs shown in zoomed insets. Control: DMSO-treated cells. The scale bar represents 10 µm. (d) Redistribution of overexpressed s3MTS-EGFP and a5NTR-EGFP in total, soluble, and insoluble fraction. β-Tubulin served as loading control.

aggregates nor co-localized with mitotracker, and was distributed diffusely in MG132-treated cells (Fig. 3ci). Interestingly, aggregates formed by proteostasis sensor protein FlucDM-EGFP were partially co-localized with mitotracker staining (Fig. 3cii). This observation could be consistent with the proposition that misfolded aggregation-prone proteins in the cytosol are imported into mitochondria for degradation [34].

When over-expressed together, Ndufs3 co-localized with Ndufa5, although mitochondrial localization of Ndufs3 was retained. This suggests a specific interaction between Ndufa5 and Ndufs3 since EGFP alone could not retain mCherry-Ndufs3 in the cytosol. Furthermore, MG132 treatment resulted in co-aggregation of both these proteins (Figs. 4a and S2f). Both the subunits were found to be ubiquitinated, and protein load was increased in the total fraction of MG132-treated cells corroborating them to be UPS substrates (Fig. 4b and c). Two bands corresponding to the precursor and mature forms of Ndufs3 were observed in the Western blotof the soluble fraction. Relative abundance of these two bands remained unchanged in MG132-treated cells, suggesting that solubility of the mature form was maintained after successful import (Fig. 4b). Interestingly, visible aggregates of EGFP-tagged Ndufa5 and Ndufs3 were not retained in the cells after 16 h of withdrawal of MG132 both in the absence and presence of protein translation blocker cycloheximide (CHX) (Fig. 4d) as opposed to 24-h MG132 treatment where the aggregates persisted (Fig. 4e). Addition of CHX ruled out any contribution of newly synthesized proteins in the reappearance of normal localization of the subunits and confirmed dissociation and reversibility of aggregates.

MG132 is known to block matrix localized Lon protease in isolated mitochondria [35]. Thus, aggregation of RCC subunits could also be resulting from the lack of Lon protease activity in MG132-treated cells. Nevertheless, both Ndufs3 and Ndufa5 consistently formed aggregates upon epoxomicin treatment (Fig. S2g), a specific proteasome inhibitor without any impact on Lon Protease [35,36], thereby confirming that aggregation of RCC subunits was exclusively due to proteostasis stress generated by proteasome inhibition. Furthermore, Ndufa5 also formed aggregates in MG132 treated HeLa cells indicating intrinsic instability of RCC subunits in response to proteostasis stress ruling out any cell line specific mechanisms (Fig. S2h). All these results together suggest that RCC subunits represent a group of highly aggregation-prone proteins that readily form aggregates upon over-expression or due to limited chaperone availability at an early stage of proteasome inhibition.

Next, we explored if RCC subunits form aggregates with similar propensity when proteostasis stress arises from different mechanisms. Hsp90 balances the cytosolic level of mitochondrial precursors by stabilizing their import-competent state or by assisting degradation [37,38]. Visible aggregation of neither Ndufa5 nor Ndufs3 was apparent by microscopy in cells treated with Hsp90 inhibitor 17-allylamino-17-demethoxygeldanamycin (17-AAG) for 8 h (Fig. S3a). However, Ndufa5 was enriched in the total and insoluble fraction confirming reduced degradation and increased insolubility (Fig. S3b). On the other hand, CHX treatment blocks production of nascent peptides in cytosol and effectively reduces substrate-load on proteostasis capacity. Expectedly, no aggregates were observed in CHX-treated cells and Ndufs3 was apparently more degradation-prone as its band intensities were reduced more than Ndufa5 (Fig. S3a and b). Carbonyl cyanide *m*-chlorophenyl hydrazone (CCCP) treatment blocks mitochondrial protein import [39]. Protein degradation is highly active in these cells to clear overload of mitochondrial precursors in cytosol [40]. Consequently, we did not see any staining of Ndufs3-EGFP outside mitochondria in CCCP-treated cells. In case of Ndufa5-EGFP, protein level was again enriched in both total and insoluble fractions suggesting less degradation and comparatively higher aggregation propensity for this protein (Fig. S3a and b).

We then treated the cells with mitochondrial-translation blocker chloramphenicol to disbalance the production of nuclear and mitochondria-encoded RCC subunits [41]. We did not see aggregates of Ndufs3 and it localized to mitochondria even after 96 h of treatment (Fig. S3c). Strikingly, several small puncta of MTS-lacking subunit Ndufa5 were observed in cytosol of both control and chloramphenicol-treated cells after 48 h. The number and size of these puncta grew further when the cells with time (96 h) (Fig. S3c). Similar small puncta of Ndufa5 appeared even at shorter time points with MG132 treatment that ultimately sequestered in large aggregates by 8 h. Ndufs3 progressively co-aggregated in these small puncta of MG132-treated cells when co-expressed with Ndufa5 (Fig. 4f). Strikingly, multiple LCR-containing proteins have recently been reported to form similar droplet-like puncta under different cellular conditions that are described as aggregate precursors [42–44].

Physicochemical properties and aggregation of RCC subunits

RCC subunits are among the comparatively abundant cellular proteins [3] and are chaperone dependent for their translocation and import into mitochondria [37,45]. However, we also identified other chaperone-dependent abundant proteins that did not necessarily increase in the insoluble fraction upon MG132 treatment. Furthermore, the heterogeneity in iBAQ values among the RCC subunits suggested that their aggregation propensity may not be correlated only with abundance (Fig. 5a). Sequence analysis showed that these proteins are physicochemically distinct with low molecular weight and basic p*I* (Fig. S4a). Out of the 21 nuclear-encoded RCC subunits found to be depleted in soluble fraction, 14 contained conventional arginine-rich MTS at the N-termini that majorly contributed to the basic p*I* of these proteins (Figs. 3a and 5b–c). In addition, these MTS sequences were overrepresented by alanine, leucine, and serine residues (Fig. 5c). More importantly, seven of these MTS sequences were predicted to contain LCRs using SEG [46] (Fig. 5b). For the remaining MTS-lacking RCC subunits that were depleted in soluble fraction, we inspected the first 30 amino acids from the N-terminus, which is the average length of MTS. Although these sequences were not rich in arginine, two of them contained LCRs and had higher percentage of threonine and serine residues (Fig. 5b and d).

N-terminal sequences of many of the nuclear-encoded RCC subunits enriched in total and insoluble fractions also contained LCRs (Fig. S4b and c). Since most of these LCRs contain multiple arginine residues,

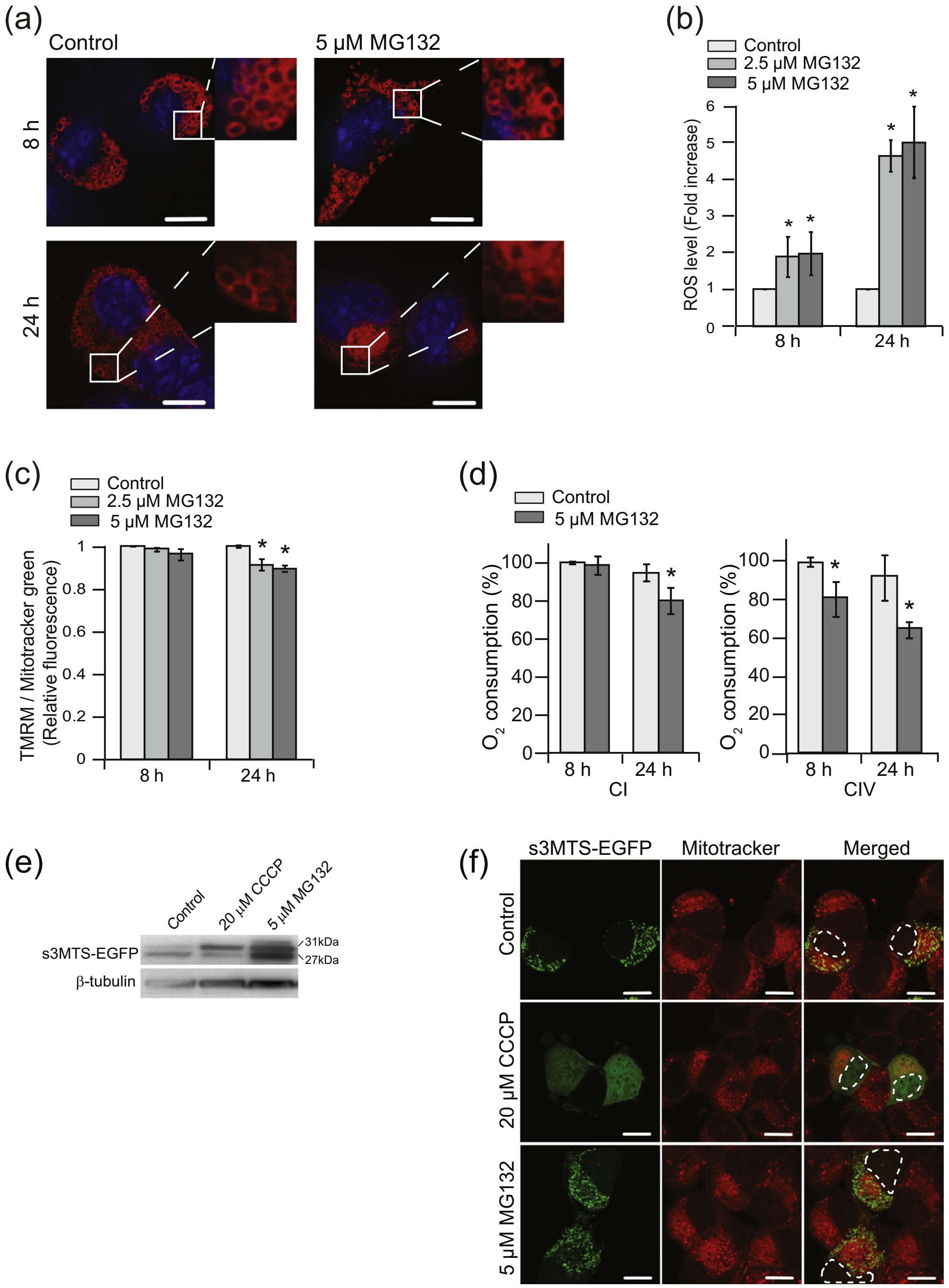

Fig. 7. Consequence of aggregation of RCC subunits—mitochondrial morphology and function. (a) Left panels: A closer look at mitochondrial morphology in untransfected MG312-treated cells for different time points. Control: DMSO-treated cells. Nucleus is stained by DAPI (blue). Digitally zoomed sections are shown as insets. (b) ROS production by MG312-treated cells for indicated time points. (c) Mitochondrial membrane potential in MG132-treated cells was evaluated by flow cytometry analysis of tetramethylrhodamine methyl ester (TMRM) fluorescence. Values are normalized on the total mitochondrial mass (Mitotracker Green fluorescence) and expressed as the TMRM fluorescence fold change. (d) Complex I and IV activity was determined on digitonin-permeabilized cells in mitochondrial respiration medium Mir05 using Oxygraph-2K. Control: DMSO-treated cells. Error bars indicate SDs from at least three independent experiments. * indicates $p < 0.05$ by Student's *t* test. (e) Immunoblot of total fraction from cells transfected with s3MTS-EGFP with simultaneous treatment of CCCP or MG132 for 24 h. β-Tubulin served as loading control. (f) Fluorescence micrographs of cells transfected with s3MTS-EGFP for 6 h followed by 8 h treatment of CCCP or MG132. Mitochondria are stained by Mitotracker CMXRos (red). Cell fixation was performed using paraformaldehyde. Nucleus is shown by dotted lines. The scale bar represents 10 μm.

these peptides are challenging to identify by trypsin-based mass spectrometry. Only two MTS peptides were identified for Ndufs7, one of which included an LCR. Both these peptides were enriched in the insoluble fraction upon MG132 treatment, suggesting that the MTS-containing precursor form of Ndufs7 is aggregation-prone (Fig. S4c).

Role of LCR containing n-terminal regions of RCC subunits in aggregation

LCRs are known to promote aggregation of many proteins. Hence, we investigated the contribution of LCRs in triggering aggregation of RCC subunits. N-terminus of Ndufs3 contained a weakly predicted LCR within the MTS (Fig. 5b). Mitochondrial import of this protein was lost upon removal of the N-terminus and ΔMTS-Ndufs3 was diffusedly distributed throughout the cytoplasm. Interestingly, the truncated construct remained aggregation-prone upon MG132 treatment (Fig. 6a). Simultaneous increase in protein level in total and insoluble fraction (Fig. 6b) suggested that removal of the weakly predicted LCR was not sufficient to prevent aggregation of Ndufs3. In contrast, when we deleted the LCR-containing N-terminal 30 amino acids from Ndufa5, the truncated version (ΔNTR-Ndufa5) did not form large aggregates anymore in the MG132-treated cells (Fig. 6a).

Addition of MTS of Ndufs3 at the N-terminus of EGFP (s3MTS-EGFP) efficiently targeted a large pool of the reporter protein to mitochondria (Fig. 6c). We did not see any increase of this chimeric protein (31 kDa) in either of the total, soluble, and insoluble fractions upon MG132 treatment. Instead, we observed a smaller band of the size of EGFP (27 kDa) in the total and soluble fraction indicating cleavage of the s3MTS after mitochondrial import. The insoluble fraction contained only the uncleaved band (31 kDa), thus suggesting instability and insolubility of the unimported cytoplasmic precursor, although its distinct aggregates were not prominently visible under the microscope (Fig. 6d).

N-terminal LCR of Ndufa5 was sufficient to trigger massive aggregation upon MG132 treatment when added before EGFP (a5NTR-EGFP). Simultaneously, protein level was also increased in the insoluble fraction of MG132-treated cells (Fig. 6c and d). In contrast, EGFP itself did not form any aggregate even upon MG132 treatment (Fig. 6c). These data together suggest LCRs are not the only determinant of aggregation of RCC subunits; physicochemical properties of the rest of the protein sequences also contribute to their aggregation.

Consequence of aggregation of RCC subunits—deregulation of respiratory function

Despite the precipitation of RCC subunits into insoluble fraction by 8-h MG132 treatment as revealed by mass spectrometry, we did not observe noticeable changes in mitochondrial morphology and membrane potential, although ROS level was increased significantly by 2-fold (Fig. 7a–c). As per high-resolution respirometry in permeabilized cells, CI-dependent oxygen flux was not significantly affected. CII function was also not perturbed; rather, a significant drop (~20%) in oxygen consumption by CIV was noticed by 8 h (Figs. 7d and S5). Nevertheless, in long-term MG132 treatment (24 h) when significant decline in cell viability was observed (Fig. 1a) and the aggregates of RCC subunits continued to accumulate (Fig. 4e), collapse of mitochondrial morphology was prominent, membrane potential had significantly dropped, and ROS level was increased by 5-fold (Fig. 7a–c). A statistically significant decrease in oxygen consumption by CI was also observed at 24 h of proteasome inhibition, and CIV activity was further reduced (Figs. 7d and S5). These results suggested that respiratory function was preserved at early stages but debilitated with the accumulation of irreversible aggregates of RCC subunits during long-term proteasome inhibition.

Finally, we checked whether aggregation RCC subunits can perturb the import of proteins into mitochondria. For this purpose, we used the reporter construct s3MTS-EGFP that spontaneously entered mitochondria (Fig. 6c). To avoid mitochondrial import of the reporter protein before proteasome inhibition, we started the MG132 treatment along with transfection. The MTS-cleaved form of s3MTS-EGFP (27 kDa) was prominently observed in Western blot of the control cells and microscopy confirmed mitochondrial localization. When we used mitochondrial transport-blocker CCCP, the precursor band intensity (31 kDa) was increased with a concomitant decrease of the MTS-cleaved form. s3MTS-EGFP was distributed diffusely throughout the CCCP-treated cells as observed by microscopy. On the other hand, MG132-treated cells showed mitochondrial localization. This indicated no blockage of mitochondrial import of s3MTS-EGFP, although both the precursor and MTS-cleaved forms were significantly accumulated in the cells after 24-h MG132 treatment (Fig. 7e and f).

Discussion

Proteostasis collapse and mitochondrial dysfunction are two hallmarks of age-related pathologies [47]. In neuronal cells, proteasome inhibition is known to deregulate mitochondrial homeostasis and turnover [48]. However, how these phenomena are coupled and what are the molecular determinants and mechanism connecting them remained to be addressed. Here, we show that RCC subunits represent a metastable subproteome that precipitates into insoluble fraction at early stages of proteasome inhibition.

Aggregation of RCC subunits is driven by diverse physicochemical signatures that normally aid their translocation or interaction into functional assemblies inside mitochondria. In recent studies, reversibility of aggregates following stress withdrawal has been described as a temporal protective measure to preserve protein function [2,49–51]. This may also be true for the reversible aggregates of RCC subunits to restore their function upon stress withdrawal. Here, we demonstrate that in the presence of prolonged stress, early aggregation of RCC subunits marks the onset of long-term proteotoxic consequences since the aggregates remain irreversible. Overall, our results suggest that early protein aggregation events during proteostasis stresses are not entirely stochastic and widespread, but rather provide predictive insights toward long-term phenotypic manifestations.

Physicochemical properties and aggregation of RCC subunits

Liquid-to-liquid and liquid-to-solid phase separations of LCR containing proteins have recently been identified as intermediary steps of their aggregation [52,53]. Here, we provide evidence that LCR-containing N-termini of multiple RCC subunits are capable of triggering aggregation of unrelated reporter proteins. In case of MTS-containing RCC subunits, increased number of positively charged arginines within N-terminal LCRs is required for interaction with the negatively charged residues of import receptors or with anionic lipids like cardiolipin on the mitochondrial membrane [45,54,55]. However, arginine-rich regions are known to trigger liquid-to-liquid phase separation followed by partitioning of proteins to insoluble fraction [56]. Alanine is another amino acid that is highly abundant within the N-terminal LCRs of MTS-containing proteins. Presence of poly-alanine stretches can also increase aggregation propensity of proteins [57]. In case of MTS-lacking RCC subunits, threonine and serine residues present within LCRs are the potential targets for phosphorylation. Interestingly, phosphorylation within LCR had been identified as a triggering factor for phase separation and aggregation of Tau [58].

We observed considerable differences between aggregation propensities of individual RCC subunits. This heterogeneity may not be attributed solely to LCRs but could be conferred by a combination of other intrinsic factors such as size, relative abundance, post-translational modifications, and amino acid sequences beyond the LCRs. Recently, many nuclear-encoded mitochondrial proteins have been shown to possess internal MTS-like signals (iMTS-LS) within the mature part of the proteins. These sequences mimic the N-terminal MTS signatures with respect to their length and amphipathicity; contain high frequencies of arginine, lysine, and hydroxylated amino acids; and are critical in maintaining the unfolded state to facilitate translocation [59]. Presence of iMTS-LS stretches may also contribute to the aggregation of RCC subunits but requires to be validated in further studies. RCC subunits, as components of large multi-subunit complexes, are likely to contain aggregation-prone interaction surfaces [60]. Indeed, our findings suggest that individual RCC subunits are aggregation-prone before their incorporation into complexes when their interaction surfaces are exposed. Thus, the unassembled RCC subunits may be considered as "orphan proteins" [61]; they lack their functional interactions when in a non-functional compartment like cytosol or when over-accumulated beyond their interaction stoichiometry with functional partners. Therefore, in addition to their physicochemical properties, aggregation of RCC subunits may also be attributed to their self-association, or loss of functional or gain of non-functional interactions with other RCC subunits, other proteins, or specific proteostasis components before their incorporation into respiratory complexes.

Proteostasis of RCC subunits

In our experiments, RCC subunits that are inherently or artificially inefficient for mitochondrial import due to lack of conventional MTS were visible outside the mitochondria. In addition, we show that association with MTS-lacking subunit Ndufa5 could partially relocalize and stabilize the otherwise efficient mitochondria-targeted subunit Ndufs3 in the cytosol. This may not be a non-specific interaction since these subunits are known to associate in a small subcomplex during complex I assembly [41]. Our findings suggest that association of these two aggregation-prone RCC subunits outside mitochondria may lead to partially folded unstable states that co-aggregate progressively during proteasome inhibition. We also identified MTS-containing precursor peptides of Ndufs7 in the insoluble fraction suggesting its aggregation even before the cleavage of MTS. Furthermore, reporter protein EGFP precipitated into insoluble fraction when LCR containing MTS of Ndufs3 was attached to its N-terminus. Incidentally, mitochondrial proteins are known to be partially unfolded and chaperone-dependent before their import [37] and proposed to be constantly degraded by proteasome in the cytosol [62]. As per our data, aggregates of RCC subunits may be present both in the cytosol and at the outer surface of mitochondria during proteasome inhibition, or even around the import channels, as described recently [32]. However, transport of MTS containing proteins to mitochondria was not blocked, suggesting that aggregates of RCC subunits did not jam the import machinery. Indeed, import of radiolabeled precursor proteins was observed to be not reduced rather improved in mitochondria isolated from proteasome-inhibited cells [62]. Thus, the fraction of RCC subunits that forms aggregates in proteasome-inhibited cells represents the excess protein load that is beyond import capacity of mitochondria. These excess RCC subunits over-accumulate in cells due to lack of degradation and form aggregates owing to their intrinsic aggregation propensity. Taken together, we propose that RCC subunits are maintained in cellular compartments at optimum concentration by chaperones and persistently degraded by the UPS to prevent their accumulation. However, if the concentration goes beyond a certain threshold and the chaperone capacity is not proportionately increased, RCC subunits clump together into aggregates.

Our experiments indicate only a marginal loss of respiratory functions at short-term proteasome inhibition, thus suggesting that functional respiratory complexes remain unperturbed despite the aggregation of RCC subunits. However, we did observe loss of respiratory functions in case of long-term proteasome inhibition. Function of respiratory complexes depends on their successful biogenesis that begins with the association of few individual RCC subunits into small sub-complexes that act as scaffolds for the coordinated and sequential incorporation of other subunits [63]. We propose that aggregation of RCC subunits at early stages of proteasome inhibition deregulates the formation of sub-complexes, and since the aggregation remains irreversible during prolonged stress, biogenesis of new respiratory complexes is damaged with prominent loss of activities.

Mitochondrial stress is known to trigger multiple defensive transcription mechanisms like mitochondrial compromised protein import response (mitoCPR) [32] or unfolded protein response (UPRmt) [64]. In this connection, investigating the possible alterations of transcription during early stages of proteasome inhibition may reveal similar defensive responses in the face of aggregation of RCC subunits. Moreover, identifying the specific chaperones and ubiquitin ligases involved in the maintenance, turnover, and import of individual RCC subunits will provide deeper understanding of the interconnectedness between progressive loss of proteostasis and bioenergetics in age-related degenerative conditions [47].

Materials and Methods

Constructs

FlucDM-EGFP was PCR-amplified from pCIneo-FlucDM-EGFP [14] and subcloned into pcDNA4/TO using the restriction enzymes KpnI and XbaI (Thermo Scientific). Ndufs3, Ndufa5, Ndufa6, and Ndufb10 were PCR-amplified from Neuro2a cDNA and cloned into pcDNA4/TO EGFP or mCherry using the restriction enzymes KpnI and XhoI. Snca was PCR-amplified from pRK172/α-synuclein [65] and cloned into pcDNA4/TO EGFP using KpnI and XhoI. The MTS or first 30 residues were removed to prepare the deletion constructs and were tagged before EGFP to prepare MTS/NTR constructs. pCI-His-hUbi was from Addgene (Plasmid No. 31815).

Cell culture and microscopy

Neuro2a cells were maintained in Dulbecco's modified Eagle's medium (Gibco) supplemented with 10% fetal bovine serum (Gibco) and 90 U/ml penicillin (Sigma)– 50 μg/ml streptomycin (Sigma) at 37 °C and 5% CO_2. Transfection of cells was performed with Lipofectamine 3000 reagent (Invitrogen) according to the manufacturer's protocol for 24 h. Mitotracker Red CMXRos (Invitrogen) staining was done at a final concentration of 0.5 mM in culture media by incubating cells for 30 min under normal growth conditions. Slides were prepared by counterstaining with DAPI (Sigma) and observed under Zeiss Axioimager Z.1 Microscope (Fig. 1d) or Leica TCS SP8 (for all other images).

For SILAC-based mass spectrometry, cells were grown in SILAC DMEM (Thermo Scientific) supplemented with 10% dialyzed fetal bovine serum (Gibco), 90 U/ml penicillin (Sigma), 50 μg/ml streptomycin (Sigma), and either light [L-lysine 2HCl/L-arginine HCl (Lys0/Arg0)] or medium [L-lysine 2HCl (4,4,5,5-D4)/L-arginine HCl ($^{13}C_6$) (Lys4/Arg6)], or heavy [L-lysine 2HCl ($^{13}C_6$, $^{15}N_2$)/L-arginine HCl ($^{13}C_6$, $^{15}N_4$) (Lys8/Arg10)] isotopes of lysine and arginine (Thermo Scientific).

Cell viability and proteasome activity assay

Cell viability was determined using MTT assay (Sigma). Briefly, 10,000 cells were plated in 96-well culture plate. After treatment, MTT solution (0.5 mg/ml in growth medium) was added followed by incubation for further 3 h under normal growth conditions. Medium was removed and formazan crystals were dissolved in DMSO. Absorbance was measured at 570 nm using PerkinElmer EnSpire Multimode plate reader.

Proteasome activity assay was performed using Proteasome-Glo Chymotrypsin-Like Cell-Based Assay kit (Promega) following the protocol described by the manufacturer. Briefly, 10,000 cells were plated in 96-well culture plate. After 8 h of MG132 treatment, pre-mixed assay buffer containing substrate and luciferin detection reagent was added in equal volume to the sample and incubated for 10 min at RT. The supernatant was transferred to optiplate-96 (white; PerkinElmer) and luminescence recorded using PerkinElmer EnSpire Multimode plate reader.

Cell death was measured using Pierce LDH Cytotoxicity Assay Kit (Thermo Scientific) as per manufacturer's protocol. Briefly, 10,000 cells were plated in 96-well culture format. After 8 h of MG132 treatment, equal volume of culture media and reaction mix was taken in a fresh plate and incubated for 30 min in dark at RT. Absorbance was recorded at 490 nm in PerkinElmer EnSpire Multimode plate reader.

Luciferase assay

Activity of FlucDM was estimated using Pierce Firefly Luciferase Glow Assay Kit (Thermo Scientific). Assay was performed as per kit protocol. Neuro2a cells were transfected with pcDNA4/TO FlucDM-EGFP using lipofectamine 3000. After 24 h, transfected cells were plated in 96-well culture plate and upon attachment were treated with 2.5 and 5 μM MG132 for 8 h and DMSO as solvent control. The cells were lysed in 100 μl of 1× lysis buffer provided in the kit, and 20 μl of this lysate was transferred into optiplate-96 (white; PerkinElmer) with 50 μl of working solution containing Luciferin. Luminescence was recorded in PerkinElmer EnSpire Multimode plate reader.

Western blotting

Cell pellet was lysed in NP-40 lysis buffer [50 mM Tris–HCl (pH 7.8), 150 mM NaCl, 1% NP-40, 0.25% sodium deoxycholate, 1 mM EDTA, protease inhibitor cocktail (Roche)] at 4 °C for 45 min with intermittent vortexing. Lysed cells were centrifuged at 12,000*g* for 15 min at 4 °C, and the supernatant was collected as the soluble fraction. The remaining pellet was washed twice with 1× PBS and boiled in 4× SDS loading buffer [0.2 M Tris–HCl (pH 6.8), 8% SDS, 0.05 M EDTA, 4% 2-mercaptoethanol, 40% glycerol, 0.8% bromophenol blue] for 15 min to get insoluble fraction. Total fraction was prepared by directly dissolving the cell pellet in 4× SDS loading buffer for 15 min. Protein fractions were separated by SDS-PAGE and transferred onto 0.2 μm PVDF membrane (Bio-Rad) for 90 min (for histones 60 min) at 300 mA using the Mini-Trans Blot cell system (Bio-Rad). Membranes were probed by appropriate primary and secondary antibodies (Supplementary Methods Table 1) and imaged using documentation system (Vilber Lourmat).

Reverse transcriptase PCR (RT-PCR)

Total RNA was prepared using Trizol method (Ambion) according to the manufacturer's protocol and treated with DNase I (Ambion). RNA concentration was measured using Nanodrop2000 spectrophotometer (Thermo Scientific). For cDNA synthesis, 2 μg of total RNA was used along with SuperScript III Reverse Transcriptase (Invitrogen) in a final volume of 20 μl according to the kit protocol. Quantitative PCR was carried out in Applied Biosystems 7900HT Fast Real-Time PCR System using Power SYBR green Master-mix (Applied Biosystems; Supplementary Methods Table 3).

Sample preparation for mass spectrometry

A total of 1.5 million cells were plated in 100-mm culture dishes. The light-labeled cells (L) served as solvent control, whereas medium-labeled (M) and heavy-labeled (h) cells were treated with 2.5 and 5 μM of MG132, respectively. After 8 h of incubation, equal number of L-, M-, and H-labeled cells were pooled together, and total, soluble, and insoluble fractions were prepared as described earlier. The fractions were separated on NuPAGE 4%–12% Bis–Tris Protein Gels (Invitrogen). The gel was run in Mes buffer (100 mM Mes, 100 mM Tris–HCl, 2 mM EDTA, 7 mM SDS) at 200 V for 40 min, fixed and stained with Coomassie brilliant blue. Preparation of gel slices, reduction, alkylation, and in-gel protein digestion was carried out as described by Shevchenko *et al*. [66]. Finally, peptides were desalted and enriched according to Rappsilber *et al*. [67].

LC–MS/MS

Peptides eluted from desalting tips were dissolved in 2% formic acid and sonicated for 5 min. Soluble fraction was analyzed on Linear Trap Quadrupole (LTQ)-OrbitrapVelos interfaced with nanoflow LC system (Easy nLC II, Thermo Scientific). Peptide fractions were separated on a Bio Basic C18 pico-Frit nanocapillary column (75 μm × 10 cm; 3 μm) using a 120-min linear gradient of the mobile phase [5% ACN containing 0.2% formic acid (buffer-A) and 95% ACN containing 0.2% formic acid (buffer-B)] at a flow rate of 300 nL/min. Full-scan MS spectra (from *m*/*z* 400 to 2000) were acquired followed by MS/MS scans of Top 20 peptides with charge states 2 or higher.

Total and insoluble fractions were analyzed on Q Exactive (Thermo Scientific) interfaced with nanoflow LC system (Easy nLC II, Thermo Scientific). Peptide fractions were separated on a Bio Basic C18 pico-Frit nanocapillary column (75 μm × 10 cm; 3 μm) using a 60-min linear gradient of the mobile phase [5% ACN containing 0.2% formic acid (buffer-A) and 95% ACN containing 0.2% formic acid (buffer-B)] at a flow rate of 400 nL/min. Full-scan MS spectra (from *m*/*z* 400 to 2000) were acquired followed by MS/MS scans of top 10 peptides with charge states 2 or higher. The mass spectrometry proteomics data of these biological repeats have been deposited to the ProteomeXchange Consortium via the PRIDE partner repository [68] with the data set identifier <PXD012204>.

Peptide identification and statistical analysis

For peptide identification, raw MS data files were loaded onto MaxQuant proteomics computational platform (Ver. 1.3.0.5) [69] and searched against Swissprot database of *Mus musculus* (release 2016.03 with 16,790 entries) and a database of known contaminants. MaxQuant used a decoy version of the specified database to adjust the false discovery rates for proteins and peptides below 1%. The search parameters included constant modification of cysteine by carbamidomethylation, enzyme specificity trypsin, and multiplicity set to 3 with Lys4 and Arg6 as medium label and Lys8 and Arg10 as heavy label. Other parameters included minimum peptide for identification 2, minimum ratio count 2, re-quantify option selected, and match between runs with 2-min time window. iBAQ [70] option was selected to compute abundance of the proteins. Bioinformatics and statistical analysis was performed in Perseus environment (Ver. 1.5.2.4) [71].

The average values from three biological repeat experiments generated as per MaxQuant algorithm were used for further analysis. For total and soluble fractions, M/L and H/L ratios were converted into log2 space, and mean ratios and standard deviations were calculated for each data set [20]. The log2 M/L and H/L ratio of each protein were converted into a *z*-score, using the following formula:

$$z-\text{score of }[\mathrm{x}] = \frac{\log_2\left(\frac{M\text{ or }H}{L}\right)[\mathrm{x}] - \text{Mean of }\ \log_2\,(a\ldots n)}{\text{Standard deviation of }\ \log_2\,(a\ldots n)}$$

where x is a single protein in the data set population (*a*…*n*). The *z*-score was a measure of how many standard deviation (σ) units, the $\log_2 M/L$, or H/L ratio of the protein was away from the population mean. A *z*-score $\geq 1.96\sigma$ represented that differential expression of the protein lied outside the 95% confidence interval and were considered to be significant. We divided the protein population into five divisions according to their *z*-score distribution. Proteins having ($-1.96 \geq z \geq 1.96$) were termed as highly depleted and highly enriched, respectively. The proteins with ($1.96 > z > 1$) or ($-1.96 < z < -1$) were classified as enriched and depleted, respectively. The proteins with ($1 \geq z \geq -1$) scores were grouped as unchanged. As insoluble fraction showed skewed distribution, mean and standard deviation of total fraction were used to normalize and calculate *z*-score. The proteins showing inconsistent ratios between 2.5 and 5 μM of MG132 treatment were removed from further analysis.

GO and bioinformatics analysis

GO analysis was performed using Gene Ontology enRIchment anaLysis and visuaLizAtion (GOrilla) tool [72]. All proteins identified in each fraction were used to prepare the respective background set with 10^{-3} as the *p* value threshold. Subcellular localization of the proteins was acquired from UniProt [73]. Protein abundance was calculated by selecting iBAQ option in MaxQuant tool. iBAQ values from the total fraction for the DMSO control (MG132 untreated) were used to calculate the relative abundances under normal conditions for the proteins identified and converted into log space. Camsol was used to predict intrinsic solubility based on the protein sequence [74]. The molecular weight and other properties of the identified proteins (p*I*, amino acid composition, hydropathicity, etc.) were taken from ProtParam (ExPASy web server) [75]. TMHMM Server v. 2.0 was used to predict transmembrane helices [76]. Low-complex regions in proteins were predicted by SEG prediction of low-complex region [46]. For prediction of mitochondrial target sequence, TPpred 2.0 online tool was used [33].

His-ubiquitin pull down assay

Cells transfected with EGFP-tagged subunits and pCI-His-hUbi were treated with 5 μM MG132 for 8 h. Cells were washed with ice-cold PBS and lysed in lysis buffer (6 M guanidine–HCl, 0.1 M Hepes (pH 7.4), 5 mM imidazole]. Ni-NTA agarose beads (Invitrogen) were equilibrated with lysis buffer and added to each cell lysate and incubated at room temperature for 2 h in a rotating wheel. Beads were washed twice with lysis buffer and four times with wash buffer [300 mM NaCl, 50 mM Tris–HCl (pH 7.4), 20 mM imidazole, 1% NP-40]. Elution was performed by boiling the beads in 2… SDS PAGE loading buffer supplemented with 300 mM imidazole for 15 min. Samples were separated on SDS-PAGE and immunoblotting was done using anti-EGFP.

High-resolution respirometry

For individual respiratory complex activities, oxygen consumption was evaluated using the substrate–uncoupler–inhibitor titration reference protocol [77] with Oxygraph-2k (Oroboros Instruments, Austria). Neuro2a cells (1×10^6 cells) were suspended in mitochondrial respiration medium Mir05 (110 mM Sucrose, 0.5 mM EGTA, 3.0 mM $MgCl_2$, 80 mM KCl, 60 mM K-lactobionate, 10 mM KH_2PO_4, 20 mM taurine, 20 mM Hepes, 1.0 g/l BSA, pH 7.1). Cells were permeabilized using digitonin (5 μg/ml) followed by respiratory complex inhibitors and substrates. Cytochrome *c* test was done to check the intactness of outer mitochondrial membrane. Oxidative phosphorylation capacity by complex I was determined by the addition of 5 mM pyruvate and 5 mM malate followed by the addition of 2.5 mM ADP. Complex II oxidative phosphorylation was measured after the addition of 0.5 μM rotenone and 10 mM succinate. Non-mitochondrial respiration was observed by addition of 2.5 μM antimycin A. For complex IV assay, 2 mM ascorbate and 0.5 mM *N*,*N*,*N*′,*N*′-tetramethyl-*p*-phenylenediamine (TMPD) were added followed by 200 mM sodium azide. All reagents were procured from Sigma.

ROS and membrane potential estimation

ROS levels were measured with Cellular ROS/Superoxide Detection Assay Kit (Abcam) as per manufacturer's protocol. Briefly, treated cells were detached and incubated with ROS Detection solution for 30 min at 37 °C in dark. Samples were analyzed using Gallios Flow Cytometer (Beckman Coulter). For mitochondrial membrane potential, treated cells were incubated with 100 μM TMRM and 50 μM Mitotracker Green for 30 min at culture conditions. Cells were detached and analyzed using Gallios Flow Cytometer (Beckman Coulter).

Acknowledgments

We thank Nitai P. Bhattacharyya, Asima Chakraborty, Somdatta Karak, and R Nagaraj for feedback on the manuscript. Proteomics facility, Advanced Microscopy and Imaging facility, Tissue culture facility and FACS facility at CSIR-CCMB provided technical assistance. We thank K Thangaraj and Rajan Kumar Jha for high-resolution respirometry experiments. Financial support from CSIR-CCMB and Max Planck Partner Group grant (M.PG.A.BIOC0003) is acknowledged. S Rawat is DBT-Senior Research Fellow. S Raychaudhuri is DBT-Ramalingaswami Fellow (BT/RLF/Re-entry/43/20 12).

Appendix A. Supplementary data

Supplementary data to this article can be found online at https://doi.org/10.1016/j.jmb.2019.01.022.

Received 20 November 2018;
Received in revised form 10 January 2019;
Accepted 11 January 2019
Available online 22 January 2019

Keywords:
proteostasis;
protein aggregation;
proteomics;
low complexity region;
respiratory chain complex

Abbreviations used:
RCC, respiratory chain complex; LCR, low-complexity region; IBs, inclusion bodies; FlucDM, firefly luciferase with double mutations; Hsf1, heat shock factor 1; GO, Gene Ontology; UPS, ubiquitin proteasome system; MTS, mitochondrial targeting sequence; CHX, cycloheximide; CCCP, carbonyl cyanide *m*-chlorophenyl hydrazone

References

[1] T.E. Audas, D.E. Audas, M.D. Jacob, J.J. Ho, M. Khacho, M. Wang, et al., Adaptation to stressors by systemic protein amyloidogenesis, Dev. Cell 39 (2016) 155–168.
[2] E.W. Wallace, J.L. Kear-Scott, E.V. Pilipenko, M.H. Schwartz, P.R. Laskowski, A.E. Rojek, et al., Reversible, specific, active aggregates of endogenous proteins assemble upon heat stress, Cell 162 (2015) 1286–1298.
[3] P. Ciryam, G.G. Tartaglia, R.I. Morimoto, C.M. Dobson, M. Vendruscolo, Widespread aggregation and neurodegenerative diseases are associated with supersaturated proteins, Cell Rep. 5 (2013) 781–790.
[4] R.M. Vabulas, S. Raychaudhuri, M. Hayer-Hartl, F.U. Hartl, Protein folding in the cytoplasm and the heat shock response, Cold Spring Harb. Perspect. Biol. 2 (2010), a004390.
[5] D.M. Walther, P. Kasturi, M. Zheng, S. Pinkert, G. Vecchi, P. Ciryam, et al., Widespread proteome remodeling and aggregation in aging C. elegans, Cell 161 (2015) 919–932.
[6] I.B. Wilde, M. Brack, J.M. Winget, T. Mayor, Proteomic characterization of aggregating proteins after the inhibition of the ubiquitin proteasome system, J. Proteome Res. 10 (2011) 1062–1072.
[7] M. Larance, Y. Ahmad, K.J. Kirkwood, T. Ly, A.I. Lamond, Global subcellular characterization of protein degradation using quantitative proteomics, Mol. Cell. Proteomics 12 (2013) 638–650.
[8] S. Bieler, S. Meiners, V. Stangl, T. Pohl, K. Stangl, Comprehensive proteomic and transcriptomic analysis reveals early induction of a protective anti-oxidative stress response by low-dose proteasome inhibition, Proteomics 9 (2009) 3257–3267.
[9] S. Bieler, E. Hammer, M. Gesell-Salazar, U. Volker, K. Stangl, S. Meiners, Low dose proteasome inhibition affects alternative splicing, J. Proteome Res. 11 (2012) 3947–3954.
[10] N. Hamdan, P. Kritsiligkou, C.M. Grant, ER stress causes widespread protein aggregation and prion formation, J. Cell Biol. 216 (2017) 2295–2304.
[11] K. Sharma, R.M. Vabulas, B. Macek, S. Pinkert, J. Cox, M. Mann, et al., Quantitative proteomics reveals that Hsp90 inhibition preferentially targets kinases and the DNA damage response, Mol. Cell. Proteomics 11 (2012) (M111 014654).
[12] K. Dasuri, P.J. Ebenezer, L. Zhang, S.O. Fernandez-Kim, R.M. Uranga, E. Gavilan, et al., Selective vulnerability of neurons to acute toxicity after proteasome inhibitor treatment: implications for oxidative stress and insolubility of newly synthesized proteins, Free Radic. Biol. Med. 49 (2010) 1290–1297.
[13] A.F. Kisselev, A.L. Goldberg, Proteasome inhibitors: from research tools to drug candidates, Chem. Biol. 8 (2001) 739–758.
[14] R. Gupta, P. Kasturi, A. Bracher, C. Loew, M. Zheng, A. Villella, et al., Firefly luciferase mutants as sensors of proteome stress, Nat. Methods 8 (2011) 879–884.
[15] S. Raychaudhuri, C. Loew, R. Korner, S. Pinkert, M. Theis, M. Hayer-Hartl, et al., Interplay of acetyltransferase EP300 and the proteasome system in regulating heat shock transcription factor 1, Cell 156 (2014) 975–985.
[16] S. Barth, D. Glick, K.F. Macleod, Autophagy: assays and artifacts, J. Pathol. 221 (2010) 117–124.
[17] W. Bao, Y. Gu, L. Ta, K. Wang, Z. Xu, Induction of autophagy by the MG132 proteasome inhibitor is associated with endoplasmic reticulum stress in MCF7 cells, Mol. Med. Rep. 13 (2016) 796–804.

[18] P. Bragoszewski, M. Turek, A. Chacinska, Control of mitochondrial biogenesis and function by the ubiquitin–proteasome system, Open Biol. 7 (2017).

[19] E. Monsellier, M. Ramazzotti, N. Taddei, F. Chiti, Aggregation propensity of the human proteome, PLoS Comput. Biol. 4 (2008), e1000199.

[20] K.M. Coombs, A. Berard, W. Xu, O. Krokhin, X. Meng, J.P. Cortens, et al., Quantitative proteomic analyses of influenza virus-infected cultured human lung cells, J. Virol. 84 (2010) 10888–10906.

[21] H. Kim, K. Heo, J. Choi, K. Kim, W. An, Histone variant H3.3 stimulates HSP70 transcription through cooperation with HP1gamma, Nucleic Acids Res. 39 (2011) 8329–8341.

[22] S. Mathivanan, R.J. Simpson, ExoCarta: a compendium of exosomal proteins and RNA, Proteomics 9 (2009) 4997–5000.

[23] J.G. Lee, S. Takahama, G. Zhang, S.I. Tomarev, Y. Ye, Unconventional secretion of misfolded proteins promotes adaptation to proteasome dysfunction in mammalian cells, Nat. Cell Biol. 18 (2016) 765–776.

[24] J. Gillis, S. Schipper-Krom, K. Juenemann, A. Gruber, S. Coolen, R. van den Nieuwendijk, et al., The DNAJB6 and DNAJB8 protein chaperones prevent intracellular aggregation of polyglutamine peptides, J. Biol. Chem. 288 (2013) 17225–17237.

[25] S. Vidoni, M.E. Harbour, S. Guerrero-Castillo, A. Signes, S. Ding, I.M. Fearnley, et al., MR-1S interacts with PET100 and PET117 in module-based assembly of human cytochrome *c* oxidase, Cell Rep. 18 (2017) 1727–1738.

[26] R. Minami, A. Hayakawa, H. Kagawa, Y. Yanagi, H. Yokosawa, H. Kawahara, BAG-6 is essential for selective elimination of defective proteasomal substrates, J. Cell Biol. 190 (2010) 637–650.

[27] S. Dennerlein, P. Rehling, Human mitochondrial COX1 assembly into cytochrome *c* oxidase at a glance, J. Cell Sci. 128 (2015) 833–837.

[28] M.E. Cheetham, A.P. Jackson, B.H. Anderton, Regulation of 70-kDa heat-shock-protein ATPase activity and substrate binding by human DnaJ-like proteins, HSJ1a and HSJ1b, Eur. J. Biochem. 226 (1994) 99–107.

[29] A. Gruber, D. Hornburg, M. Antonin, N. Krahmer, J. Collado, M. Schaffer, et al., Molecular and structural architecture of polyQ aggregates in yeast, Proc. Natl. Acad. Sci. U. S. A. 115 (2018) E3446–E3453.

[30] D.C. David, N. Ollikainen, J.C. Trinidad, M.P. Cary, A.L. Burlingame, C. Kenyon, Widespread protein aggregation as an inherent part of aging in *C. elegans*, PLoS Biol. 8 (2010), e1000450.

[31] R.O. Vogel, C.E. Dieteren, L.P. van den Heuvel, P.H. Willems, J.A. Smeitink, W.J. Koopman, et al., Identification of mitochondrial complex I assembly intermediates by tracing tagged NDUFS3 demonstrates the entry point of mitochondrial subunits, J. Biol. Chem. 282 (2007) 7582–7590.

[32] H. Weidberg, A. Amon, MitoCPR-A surveillance pathway that protects mitochondria in response to protein import stress, Science 360 (2018).

[33] C. Savojardo, P.L. Martelli, P. Fariselli, R. Casadio, TPpred2: improving the prediction of mitochondrial targeting peptide cleavage sites by exploiting sequence motifs, Bioinformatics 30 (2014) 2973–2974.

[34] L. Ruan, C. Zhou, E. Jin, A. Kucharavy, Y. Zhang, Z. Wen, et al., Cytosolic proteostasis through importing of misfolded proteins into mitochondria, Nature 543 (2017) 443–446.

[35] A. Bayot, N. Basse, I. Lee, M. Gareil, B. Pirotte, A.L. Bulteau, et al., Towards the control of intracellular protein turnover: mitochondrial Lon protease inhibitors versus proteasome inhibitors, Biochimie 90 (2008) 260–269.

[36] A. Bezawork-Geleta, E.J. Brodie, D.A. Dougan, K.N. Truscott, LON is the master protease that protects against protein aggregation in human mitochondria through direct degradation of misfolded proteins, Sci. Rep. 5 (2015) 17397.

[37] J.C. Young, N.J. Hoogenraad, F.U. Hartl, Molecular chaperones Hsp90 and Hsp70 deliver preproteins to the mitochondrial import receptor Tom70, Cell 112 (2003) 41–50.

[38] D.H. Margineantu, C.B. Emerson, D. Diaz, D.M. Hockenbery, Hsp90 inhibition decreases mitochondrial protein turnover, PLoS One 2 (2007), e1066.

[39] A. Geissler, T. Krimmer, U. Bomer, B. Guiard, J. Rassow, N. Pfanner, Membrane potential-driven protein import into mitochondria. The sorting sequence of cytochrome *b*(2) modulates the deltapsi-dependence of translocation of the matrix-targeting sequence, Mol. Biol. Cell 11 (2000) 3977–3991.

[40] L. Wrobel, U. Topf, P. Bragoszewski, S. Wiese, M.E. Sztolsztener, S. Oeljeklaus, et al., Mistargeted mitochondrial proteins activate a proteostatic response in the cytosol, Nature 524 (2015) 485–488.

[41] S. Guerrero-Castillo, F. Baertling, D. Kownatzki, H.J. Wessels, S. Arnold, U. Brandt, et al., The assembly pathway of mitochondrial respiratory chain complex I, Cell Metab. 25 (2017) 128–139.

[42] A.R. Strom, A.V. Emelyanov, M. Mir, D.V. Fyodorov, X. Darzacq, G.H. Karpen, Phase separation drives heterochromatin domain formation, Nature 547 (2017) 241–245.

[43] S. Qamar, G. Wang, S.J. Randle, F.S. Ruggeri, J.A. Varela, J.Q. Lin, et al., FUS phase separation is modulated by a molecular chaperone and methylation of arginine cation–pi interactions, Cell 173 (2018) 720–734 (e15).

[44] T.M. Franzmann, M. Jahnel, A. Pozniakovsky, J. Mahamid, A.S. Holehouse, E. Nuske, et al., Phase separation of a yeast prion protein promotes cellular fitness, Science 359 (2018) 1–8.

[45] M. Kunze, J. Berger, The similarity between N-terminal targeting signals for protein import into different organelles and its evolutionary relevance, Front. Physiol. 6 (2015) 259.

[46] J.C. Wootton, Non-globular domains in protein sequences: automated segmentation using complexity measures-Comput. Chem. 18 (1994) 269–285.

[47] C. Lopez-Otin, M.A. Blasco, L. Partridge, M. Serrano, G. Kroemer, The hallmarks of aging, Cell 153 (2013) 1194–1217.

[48] P.G. Sullivan, N.B. Dragicevic, J.H. Deng, Y. Bai, E. Dimayuga, Q. Ding, et al., Proteasome inhibition alters neural mitochondrial homeostasis and mitochondria turnover, J. Biol. Chem. 279 (2004) 20699–20707.

[49] S. Kroschwald, S. Alberti, Gel or die: phase separation as a survival strategy, Cell 168 (2017) 947–948.

[50] J.A. Riback, C.D. Katanski, J.L. Kear-Scott, E.V. Pilipenko, A.E. Rojek, T.R. Sosnick, et al., Stress-triggered phase separation is an adaptive, evolutionarily tuned response, Cell 168 (2017) 1028–1040 (e19).

[51] R. Narayanaswamy, M. Levy, M. Tsechansky, G.M. Stovall, J.D. O'Connell, J. Mirrielees, et al., Widespread reorganization of metabolic enzymes into reversible assemblies upon nutrient starvation, Proc. Natl. Acad. Sci. U. S. A. 106 (2009) 10147–10152.

[52] S. Wegmann, B. Eftekharzadeh, K. Tepper, K.M. Zoltowska, R.E. Bennett, S. Dujardin, et al., Tau protein liquid–liquid phase separation can initiate tau aggregation, EMBO J. 37 (2018).

[53] T.R. Peskett, F. Rau, J. O'Driscoll, R. Patani, A.R. Lowe, H.R. Saibil, A liquid to solid phase transition underlying pathological huntingtin exon1 aggregation, Mol. Cell 70 (2018) 588–601 (e6).

[54] A.B. Harbauer, R.P. Zahedi, A. Sickmann, N. Pfanner, C. Meisinger, The protein import machinery of mitochondria—a regulatory hub in metabolism, stress, and disease, Cell Metab. 19 (2014) 357–372.

[55] K. Pfeiffer, V. Gohil, R.A. Stuart, C. Hunte, U. Brandt, M.L. Greenberg, et al., Cardiolipin stabilizes respiratory chain supercomplexes, J. Biol. Chem. 278 (2003) 52873–52880.

[56] S. Boeynaems, E. Bogaer`t, D. Kovacs, A. Konijnenberg, E. Timmerman, A. Volkov, et al., Phase separation of C9orf72 dipeptide repeats perturbs stress granule dynamics, Mol. Cell 65 (2017) 1044–1055 (e5).

[57] I. Pelassa, D. Cora, F. Cesano, F.J. Monje, P.G. Montarolo, F. Fiumara, Association of polyalanine and polyglutamine coiled coils mediates expansion disease-related protein aggregation and dysfunction, Hum. Mol. Genet. 23 (2014) 3402–3420.

[58] S. Ambadipudi, J. Biernat, D. Riedel, E. Mandelkow, M. Zweckstetter, Liquid–liquid phase separation of the microtubule-binding repeats of the Alzheimer-related protein tau, Nat. Commun. 8 (2017) 275.

[59] S. Backes, S. Hess, F. Boos, M.W. Woellhaf, S. Godel, M. Jung, et al., Tom70 enhances mitochondrial preprotein import efficiency by binding to internal targeting sequences, J. Cell Biol. 217 (2018) 1369–1382.

[60] S. Pechmann, E.D. Levy, G.G. Tartaglia, M. Vendruscolo, Physicochemical principles that regulate the competition between functional and dysfunctional association of proteins, Proc. Natl. Acad. Sci. U. S. A. 106 (2009) 10159–10164.

[61] S. Juszkiewicz, R.S. Hegde, Quality control of orphaned proteins, Mol. Cell 71 (2018) 443–457.

[62] P. Bragoszewski, A. Gornicka, M.E. Sztolsztener, A. Chacinska, The ubiquitin–proteasome system regulates mitochondrial intermembrane space proteins, Mol. Cell. Biol. 33 (2013) 2136–2148.

[63] A. Melber, D.R. Winge, Inner secrets of the respirasome, Cell 167 (2016) 1450–1452.

[64] A. Melber, C.M. Haynes, UPR(mt) regulation and output: a stress response mediated by mitochondrial-nuclear communication, Cell Res. 28 (2018) 281–295.

[65] M.F. Ahmad, T. Ramakrishna, B. Raman, Ch.M. Rao, Fibrillogenic and non-fibrillogenic ensembles of SDS-bound human alpha-synuclein, J. Mol. Biol. 364 (2006) 1061–1072.

[66] A. Shevchenko, M. Wilm, O. Vorm, M. Mann, Mass spectrometric sequencing of proteins silver-stained polyacrylamide gels, Anal. Chem. 68 (1996) 850–858.

[67] J. Rappsilber, Y. Ishihama, M. Mann, Stop and go extraction tips for matrix-assisted laser desorption/ionization, nanoelectrospray, and LC/MS sample pretreatment in proteomics, Anal. Chem. 75 (2003) 663–670.

[68] J.A. Vizcaino, E.W. Deutsch, R. Wang, A. Csordas, F. Reisinger, D. Rios, et al., ProteomeXchange provides globally coordinated proteomics data submission and dissemination, Nat. Biotechnol. 32 (2014) 223–226.

[69] J. Cox, M. Mann, MaxQuant enables high peptide identification rates, individualized p.p.b.-range mass accuracies and proteome-wide protein quantification, Nat. Biotechnol. 26 (2008) 1367–1372.

[70] B. Schwanhausser, D. Busse, N. Li, G. Dittmar, J. Schuchhardt, J. Wolf, et al., Global quantification of mammalian gene expression control, Nature 473 (2011) 337–342.

[71] S. Tyanova, T. Temu, P. Sinitcyn, A. Carlson, M.Y. Hein, T. Geiger, et al., The Perseus computational platform for comprehensive analysis of (prote)omics data, Nat. Methods 13 (2016) 731–740.

[72] E. Eden, R. Navon, I. Steinfeld, D. Lipson, Z. Yakhini, GOrilla: a tool for discovery and visualization of enriched GO terms in ranked gene lists, BMC Bioinforma. 10 (2009) 48.

[73] R. Apweiler, A. Bairoch, C.H. Wu, W.C. Barker, B. Boeckmann, S. Ferro, et al., UniProt: the universal protein knowledgebase, Nucleic Acids Res. 32 (2004) D115–D119.

[74] P. Sormanni, F.A. Aprile, M. Vendruscolo, The CamSol method of rational design of protein mutants with enhanced solubility, J. Mol. Biol. 427 (2015) 478–490.

[75] E. Gasteiger, C. Hoogland, A. Gattiker, S. Duvaud, M.R. Wilkins, R.D. Appel, et al., Protein identification and analysis tools on the ExPASy server, in: J.M. Walker (Ed.), The Proteomics Protocols Handbook, Humana Press, 2005.

[76] A. Krogh, B. Larsson, G. von Heijne, E.L. Sonnhammer, Predicting transmembrane protein topology with a hidden Markov model: application to complete genomes, J. Mol. Biol. 305 (2001) 567–580.

[77] D. Pesta, E. Gnaiger, High-resolution respirometry: OXPHOS protocols for human cells and permeabilized fibers from small biopsies of human muscle, Methods Mol. Biol. 810 (2012) 25–58.